



Nanoscale

---

**Optically induced trion formation and its control in  
MoS<sub>2</sub>/graphene van der Waals heterostructure**

Journal:	<i>Nanoscale</i>
Manuscript ID	NR-ART-05-2024-002078.R2
Article Type:	Paper
Date Submitted by the Author:	25-Aug-2024
Complete List of Authors:	Ghosh Dastidar, Madhura; Indian Institute of Technology Madras, Physics Basu, Nilanjan; Ulsan National Institute of Science and Technology, Chemistry Kao, I-Hsuan; Carnegie Mellon University, Department of Physics Katoch, Jyoti; Carnegie Mellon University Nayak, Pramoda; Jain University; Indian Institute of Technology Madras Singh, Simranjeet; Carnegie Mellon University Bhallamudi, Vidya Praveen; Indian Institute of Technology Madras,

SCHOLARONE™  
Manuscripts

Cite this: DOI: 00.0000/xxxxxxxxxx

# Optically induced trion formation and its control in MoS<sub>2</sub>/graphene van der Waals heterostructure

Madhura Ghosh Dastidar<sup>a,b,c</sup>, Nilanjan Basu<sup>a,b,c</sup>, I-Hsuan Kao<sup>d</sup>, Jyoti Katoch<sup>d</sup>, Pramoda K. Nayak<sup>†a,c,e</sup>, Simranjeet Singh<sup>d</sup> and Vidya Praveen Bhallamudi<sup>\*a,b</sup>

Received Date

Accepted Date

DOI: 00.0000/xxxxxxxxxx

Monolayer 2D transition metal dichalcogenides (TMDs) show high sensitivity to the local dielectric environment, leading to modulation of their optoelectronic properties. Here, we report on the formation of localized trions in MoS<sub>2</sub>/few-layer graphene van der Waals' heterostructure. We performed temperature-dependent photoluminescence and Raman studies down to 80 K, to understand the mechanism for localized charge excitation, which shows contrasting behaviour with MoS<sub>2</sub>/SiO<sub>2</sub>. We attribute trion formation to optically-induced charge transfer from few-layer graphene to MoS<sub>2</sub>. Our theoretical analysis and simulations comparing the dielectric screening between MoS<sub>2</sub>/SiO<sub>2</sub> and MoS<sub>2</sub>/few-layer graphene, strongly suggest the dominance of excess charge carrier concentration over dielectric screening as the cause for trion formation. The concentration of charge carriers could be tuned actively with excitation power. Our findings provide an efficient approach for trion formation in MoS<sub>2</sub> and explicate the mechanism behind charge transfer in the MoS<sub>2</sub>/few-layer graphene heterostructure.

## 1 Introduction

Layered TMDs in their 2D forms exhibit bandgaps in the 1-2 eV range which can undergo a transition from an indirect to a direct band gap in the single layer limit. This has generated a lot of interest in these materials yielding applications in photonics and optoelectronics<sup>1</sup>. Being a semiconductor, monolayer MoS<sub>2</sub> has a low dielectric constant ( $K \sim 5$ ) and therefore weak dielectric screening<sup>2</sup>, allowing strong Coulomb interactions among the carriers. This results in the formation of many-body states such as excitons (electron-hole pairs) and trions<sup>3,4</sup>, at above-cryogenic temperatures. In contrast to excitons, a trion possesses a net charge and spin, which allows for spin-dependent studies<sup>5</sup> and optical probing of the local electrostatic variation<sup>6</sup>. Trions have been intensively explored for a broad range of potential applications, including quantum information<sup>5</sup>, sensing<sup>6</sup>, lasing<sup>7</sup>, and light-emitting devices<sup>8</sup>. Further, these quasiparticles in TMDs

have binding energy orders of magnitude larger than conventional semiconductors<sup>9</sup>.

The formation of trions can be observed from the photoluminescence (PL) of monolayer MoS<sub>2</sub>, providing information about the carrier concentration in the material. Few-layer graphene (FLG) is an important van-der Waal's material with rich electron concentration<sup>10</sup>. It also has better charge transfer efficiency compared to monolayer graphene and is robust for forming heterostructure. Further, stacking two different van der Waal's materials allows one to tune the electrical and optical properties of the system, which may be unlike both constituent materials. Since the semiconducting or 2H phase of MoS<sub>2</sub> has a controllable conductivity<sup>11</sup>, it is suitable for practical optoelectronics due to its good energy cycling stability and well-studied synthesis procedure<sup>12,13</sup>. To achieve better conductivity alongside optical sensitivity, MoS<sub>2</sub> can be stacked on top of few-layer graphene without altering its Dirac cone<sup>14</sup>.

Existing research on MoS<sub>2</sub>/FLG based heterostructures has been performed in the context of electrical applications<sup>15–18</sup>. The optical readout of the quasiparticles in MoS<sub>2</sub> has been performed mostly as a function of electrostatic gating, through which charged excitons were manipulated. In most cases, trions in TMDs are either found naturally or formed in a controlled manner by ion implantation<sup>19</sup>, doping chemically<sup>20</sup> or electrically, etc<sup>4</sup>. Chemical and implantation methods may degrade the sample quality and do not provide active control over the carrier concentration. Trion binding energies in the range of tens of

<sup>a</sup> Department of Physics, Indian Institute of Technology Madras, Chennai 600036, India

<sup>b</sup> Quantum Centers in Diamond and Emerging Materials (QuCenDiEM) Group, Department of Electrical Engineering, Indian Institute of Technology Madras, Chennai 600036, India

<sup>c</sup> 2D Materials Research and Innovation Group, Indian Institute of Technology Madras, Chennai 600036, India

<sup>d</sup> Department of Physics, Carnegie Mellon University, Pittsburgh, PA, 15213, USA

<sup>e</sup> Centre for Nano and Material Sciences, Jain (Deemed-to-be University), Jain Global Campus, Kanakapura, Bangalore 562112, Karnataka, India

<sup>†</sup> pramoda.nayak@jainuniversity.ac.in

<sup>\*</sup> praveen.bhallamudi@iitm.ac.in

meVs<sup>4,21–24</sup> have been reported in literature for monolayer MoS<sub>2</sub> on SiO<sub>2</sub>. Thus, trion dynamics can be better elucidated at lower temperatures than 300 K, due to reduced phonon scattering. Understanding the behaviour of the quasiparticles under optical excitation has not been explored thoroughly for the MoS<sub>2</sub>/FLG heterostructure. Further, most reports use electrostatic gating as the control over trion concentration in MoS<sub>2</sub>.

In this work, we present the temperature-dependent behaviour of negatively charged trions observed in MoS<sub>2</sub> stacked on few-layer graphene, via optical readout. Raman and PL spectroscopy have been used as reliable techniques to measure carrier concentration in monolayer MoS<sub>2</sub>. In-situ, confocal Raman and PL studies have been performed as a function of temperature for studying the dynamics of the photocarriers in MoS<sub>2</sub> when supported by FLG and SiO<sub>2</sub>/Si. We observe selective trion formation in MoS<sub>2</sub> on FLG, which is interestingly absent in MoS<sub>2</sub>/SiO<sub>2</sub> (part of the same heterostructure). We use the temperature-dependent mass action law to quantify the binding energy of trions ( $\approx 15$  meV) and carrier concentration ( $\approx 10^{10}$  cm<sup>-2</sup>) using our experimental data. We show that the power of the optical excitation can be used as a knob for the control over trion concentration.

## 2 Results

### 2.1 Sample Structure and Raman Spectra

The schematic and the optical image of as-prepared heterostructure is shown in Figs. 1 (a)-(b). The CVD-grown monolayer MoS<sub>2</sub> flake (top triangle, 0.95 nm thickness see Fig. S1 in the supplementary information) lies on a graphite flake ( $\approx 4$  nm thick, hence referred to as few-layer graphene). We have denoted the two different spots of MoS<sub>2</sub> where confocal optical measurements were conducted on the sample (sample 1) – MoS<sub>2</sub>/SiO<sub>2</sub> (S<sub>1</sub>: Spot 1) and MoS<sub>2</sub>/FLG (S<sub>3</sub>: Spot 3) [see Supplementary Information].

For characterizing the sample, Raman spectral measurements conducted on MoS<sub>2</sub> flake (see Fig. 1 (b) for measurement spots) of the heterostructure at room temperature, are shown in Fig. 1 (c). The characteristic Raman modes of MoS<sub>2</sub> corresponding to in-plane (E<sub>2g</sub>) and out-of-plane vibration (A<sub>1g</sub>) are seen at wavenumbers  $\approx 385$  and  $\approx 405$  cm<sup>-1</sup><sup>25</sup>, respectively. For a material placed on top of few-layer graphene, the Raman signal can be even weaker than SiO<sub>2</sub>/Si as the substrate<sup>26</sup>. Thus, we observe a weaker Raman signal from MoS<sub>2</sub>/FLG as compared to MoS<sub>2</sub>/SiO<sub>2</sub>. The Raman spectral measurement for FLG was performed at 300 K. We obtained the modes at 1580 cm<sup>-1</sup> (G peak) and 2718 cm<sup>-1</sup> (2D peak), which are consistent with earlier reports for pristine, undoped FLG<sup>27</sup>. The supplementary information contains the said Raman spectra [Fig. S2].

### 2.2 Trion formation: Evidence, Temperature-dependence and Optical Control

An exciton can acquire a negative or positive charge by interacting with an electron or hole, respectively, to form trions. Like excitons, trions also undergo radiative decay, wherein an electron or hole is removed from the quasiparticle with a considerable amount of momentum, leaving the net-zero momentum charge pair to recombine. Due to differences in their recombination en-

ergies, excitons and trions emit optical light having slightly different wavelengths [see Fig. 2 (a) and Fig. S3 in the supplementary information]. Further, since the binding energies of the quasiparticles are comparable to room temperature, the bound state wave function and thermal momentum distribution of trions can be changed by varying the temperature.

To understand the substrate-dependent effects<sup>18</sup> on the emission properties of the heterostructure, we perform a temperature-dependent confocal photoluminescence (PL) measurement on the spots: MoS<sub>2</sub>/SiO<sub>2</sub> (S<sub>1</sub>) and MoS<sub>2</sub>/FLG (S<sub>3</sub>) for sample 1. While we present data for only these two spots, we have performed the same measurements for two different samples and on various spots. This is done to check the reproducibility of our results, as shown in the supplementary information Figs. S5-S7. While some details may change, the key analysis and conclusions are supported by the other spots/data.

In Fig. 2 (b), we present the PL spectra recorded on MoS<sub>2</sub>/SiO<sub>2</sub> and MoS<sub>2</sub>/FLG at 79 K. For MoS<sub>2</sub>/SiO<sub>2</sub> we see a peak at 1.91 eV. This corresponds to the well-studied A exciton peak<sup>28</sup> and is observed at 1.83 eV<sup>29</sup> (from our measurements as well), at room temperature. For MoS<sub>2</sub>/FLG we see an asymmetric main peak, which can be deconvolved into two peaks. We attribute the higher energy one (1.94 eV) to the A exciton peak and the lower energy peak (1.92 eV) to trions. An asymmetric peak may be observed due to other effects, such as modulation of distance from the substrate or other substrate-induced effects<sup>30</sup>. However, we rule these out based on further data and analysis presented later. More detailed reasoning can be found in the Supplementary Information (Sec. 4). We also observe the B exciton peak in the MoS<sub>2</sub>/SiO<sub>2</sub> and MoS<sub>2</sub>/FLG data as well (see Fig. S4 of Supplementary Information). However, we do not analyze the B peak further in our study, as they do not affect the trion formation in our samples that we seek to understand. Please note that we will refer to A exciton peak as exciton peak in this work.

We perform temperature-dependent (79-300 K) PL studies to understand the origin and behaviour of these peaks. In Fig. 2 (c) and (d), the measured temperature-dependent PL spectra are shown for MoS<sub>2</sub>/FLG and MoS<sub>2</sub>/SiO<sub>2</sub>, respectively. The fittings for the complete datasets are shown in the Supplementary Information (SI) [see Fig. S8]. With the increase in temperature, the overall spectra show a lowering of peak energies for MoS<sub>2</sub>/SiO<sub>2</sub> and MoS<sub>2</sub>/FLG, which occurs due to the thermal expansion of the lattice<sup>31,32</sup>. While the dual peaks seen in the PL spectra of MoS<sub>2</sub>/FLG at 79 K are not as clearly visible at temperatures  $> 160$  K, the two peaks are present and can be seen in the asymmetry of the convoluted peak. The PL spectra for MoS<sub>2</sub>/SiO<sub>2</sub> at various temperatures show no substantial asymmetry on the lower energy end. The asymmetry observed for MoS<sub>2</sub>/SiO<sub>2</sub> on the higher energy end is described as follows. The PL spectra of TMDCs comprise contributions from excitons with zero center-of-mass momentum and phonon sidebands of dark excitons with finite momenta<sup>28</sup>. The former decays radiatively resulting in symmetric PL profiles (without any tail). At non-zero temperatures, the excitons occupy the energy states following the Maxwell-Boltzmann distribution. Thus phonon-assisted recombinations of the excitons which have non-zero momenta lead to the tail on the higher-

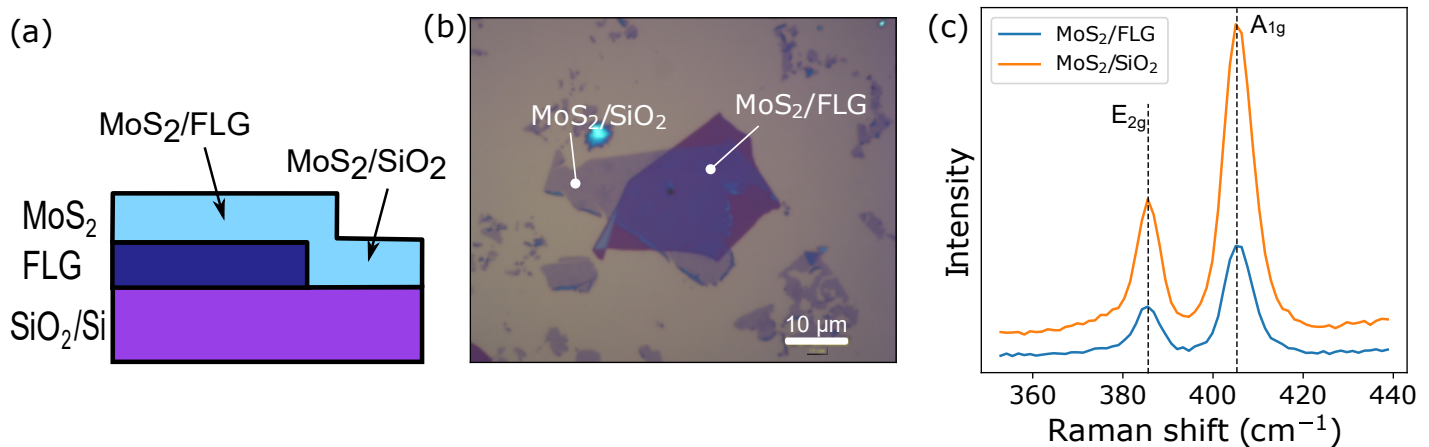


Fig. 1 Characterization of the heterostructure: (a) Schematic of the MoS<sub>2</sub>/FLG heterostructure showing the different portions. The heterostructure comprises a portion with MoS<sub>2</sub> on few-layer graphene and MoS<sub>2</sub> on 300 nm SiO<sub>2</sub>/Si substrate denoted as MoS<sub>2</sub>/FLG and MoS<sub>2</sub>/SiO<sub>2</sub>, respectively. (b) Optical micrograph of the MoS<sub>2</sub>/FLG heterostructure, scale bar: 10 μm. The white dots denote the positions where confocal Raman spectral measurements were conducted for MoS<sub>2</sub>/FLG and MoS<sub>2</sub>/SiO<sub>2</sub>. (c) Raman spectra measured for MoS<sub>2</sub>/SiO<sub>2</sub> (orange) and MoS<sub>2</sub>/FLG (blue) which are each part of the same MoS<sub>2</sub>/FLG heterostructure [measurement locations shown in (b)] measured at 300 K. The two Raman modes corresponding to in-plane and out-of-plane vibrations is denoted by E<sub>2g</sub> and A<sub>1g</sub>, respectively, and their peak centers are marked using dashed lines.

energy end of the PL spectra and cannot be considered as evidence for trions. Thus, we do not see significant trion formation in MoS<sub>2</sub>/SiO<sub>2</sub> in contrast to previous reports<sup>28</sup>, when compared to MoS<sub>2</sub>/FLG. This could be due to the increase of neutral photo-carriers in MoS<sub>2</sub><sup>4,33</sup> on FLG, which indicates photoinduced charge transfer in MoS<sub>2</sub> via few-layer graphene. We deconvolve the two peaks for every temperature and extract quantitative information about the PL spectra.

The spectral red-shift (mentioned earlier) and the increase in each peak's FWHM with temperature for MoS<sub>2</sub>/SiO<sub>2</sub> and MoS<sub>2</sub>/FLG are quantified in Fig. S9 (a)-(b). In the case of MoS<sub>2</sub>/FLG, the trion peak's intensity keeps increasing with a decrease in temperature, whereas the excitons follow a non-monotonic behaviour [see Fig. 3 (a)]. To understand the contribution to PL from these excitons and trions, the integrated PL area was plotted with temperature for both portions of the heterostructure in Fig. 3 (b). We observe that the integrated PL area shows a drastic increase for MoS<sub>2</sub>/SiO<sub>2</sub> whereas for MoS<sub>2</sub>/FLG, it remains approximately constant. The constancy in the PL area for MoS<sub>2</sub>/FLG can be attributed to the conversion of excitons to trions in MoS<sub>2</sub> due to the presence of excess electrons. The conversion from excitons to trions requires some non-radiative energy intake from the incident photons, due to momentum conservation<sup>34</sup>. Thus, the emergence of the trion peak (overlapped with the exciton peak) keeps PL area relatively constant for MoS<sub>2</sub>/FLG at various temperatures.

To provide an active control on the trion concentration in MoS<sub>2</sub>/FLG, we perform a power-dependent PL measurement for 4 different temperatures on the heterostructure. It is observed that even if the laser power is increased, trion formation does not take place in MoS<sub>2</sub>/SiO<sub>2</sub> [see Fig. S10 in SI]. First, we observe that the peak intensities for both excitons (I<sub>A</sub>) and trions (I<sub>T</sub>) increase with incident power [see Fig. 4 (a)-(b)]. The power law fittings ( $\sim P^\alpha$ ) have been shown which agree with the expected trends for excitons and trions<sup>21,35–38</sup> [see Figs. 4(a) and (b)]. We

obtained the power law  $\approx P^\alpha$ , where  $\alpha \approx 0.9$  and  $\alpha \approx 1.2$  for exciton and trion recombinations as a function of laser power density, respectively, for all temperatures other than 300 K. This matches with the expected trends for exciton and trion intensities as a function of incident power. At 300 K, trion concentration is low, owing to its smaller binding energy. Thus, the power law follows the behaviour for exciton recombination which is more prominent. In literature, a range of  $\alpha$  from 0.8 - 1 and 1 - 1.5<sup>21,35–38</sup> are reported for the power laws obeyed by excitons and trions, respectively. Next, we plot  $I_T/I_A$  as a function of incident power for MoS<sub>2</sub>/FLG in Fig. 4 (c) and observe its increase with temperature. Using Eq. 4 (derived in Sec. 2.3) we fit the measured datasets of  $I_T/I_A$  vs. laser power density for 4 different temperatures as shown in Fig. 4. An increase in  $I_T/I_A$  indicates the control of trion concentration in MoS<sub>2</sub>/FLG via incident laser power.

### 2.3 Mass Action Model: extracting trion concentration

To determine the relative intensity of the two quasiparticle systems (trion spectral weight,  $I_T/I_A$ ) from their PL signals, a dynamical model is adopted. Let  $n_T$ ,  $n_A$ , and  $n_e$  denote the concentrations of trions, A excitons and free electrons, respectively. Further, let  $n_P = n_A + n_T$  and  $n_B = n_T + n_e$  denote the concentrations of photocarriers generated by the laser and the doping level before, respectively. Now, the reaction for trion formation is  $A + e^- \rightarrow T$ . From the law of mass action<sup>23,39</sup>,

$$\frac{n_A n_e}{n_T} = C_1 k_B T \exp\left\{-\frac{E_b^T}{k_B T}\right\} \quad (1)$$

where  $T$  is the temperature,  $k_B$  is the Boltzmann constant,  $E_b^T$  is the trion binding energy and  $C_1 = \frac{16\pi M_A m_e}{h^2 M_T}$ , in which  $M_T = 2m_e + m_h$  and  $M_A = m_e + m_h$ ,  $m_e$  [ $m_h$ ] is the electron [hole] mass. At a fixed temperature  $T$ , we can write the above equation as:

$$\frac{n_A n_e}{n_T} = C(T) \quad (2)$$

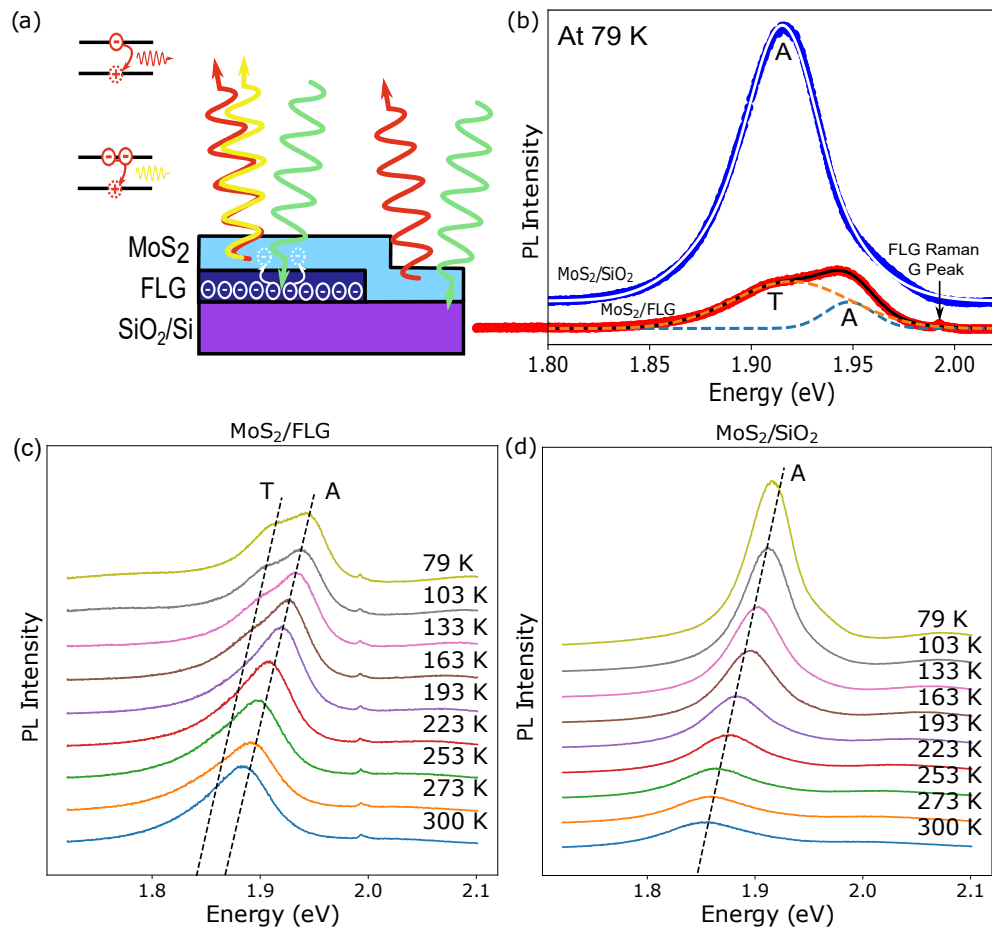


Fig. 2 Evidence of trion formation in MoS<sub>2</sub>/FLG: (a) Schematic of the processes of optical emission from the different portions of the MoS<sub>2</sub>/FLG heterostructure, when excited with 532 nm light. Charge transfer from FLG upon illumination can support trion formation selectively on the MoS<sub>2</sub>/FLG, which shows up as a second peak in the PL in addition to the exciton peaks. (b) Comparison of the MoS<sub>2</sub> PL measured (dots) and fitted (solid and dashed lines) at 79 K for SiO<sub>2</sub>/Si [top, blue curve] and FLG [bottom, red curve] on the same scale. This is performed by dividing all spectra with the maximum intensity of MoS<sub>2</sub>/SiO<sub>2</sub> [blue curve] at 79 K. The fittings show the convolution of two Gaussians corresponding to exciton (A) and trion (T) peaks in MoS<sub>2</sub>/FLG, as opposed to only an excitonic peak (A) in MoS<sub>2</sub>/SiO<sub>2</sub>. A manual offset is added to MoS<sub>2</sub>/SiO<sub>2</sub> PL to stack it over MoS<sub>2</sub>/FLG for clear visibility. The sharp peak indicates the Raman peak of FLG for the G mode (1580 cm<sup>-1</sup> which is ~ 580 nm for 532 nm excitation). (c) and (d) show the temperature-dependent spectra for MoS<sub>2</sub>/FLG and MoS<sub>2</sub>/SiO<sub>2</sub>, respectively. The PL intensities for both MoS<sub>2</sub>/FLG and MoS<sub>2</sub>/SiO<sub>2</sub> are plotted on the same scale, performed by dividing all spectra with the maximum intensity of MoS<sub>2</sub>/SiO<sub>2</sub> at 79 K. A manual offset is then added to stack the spectra for clear visibility.

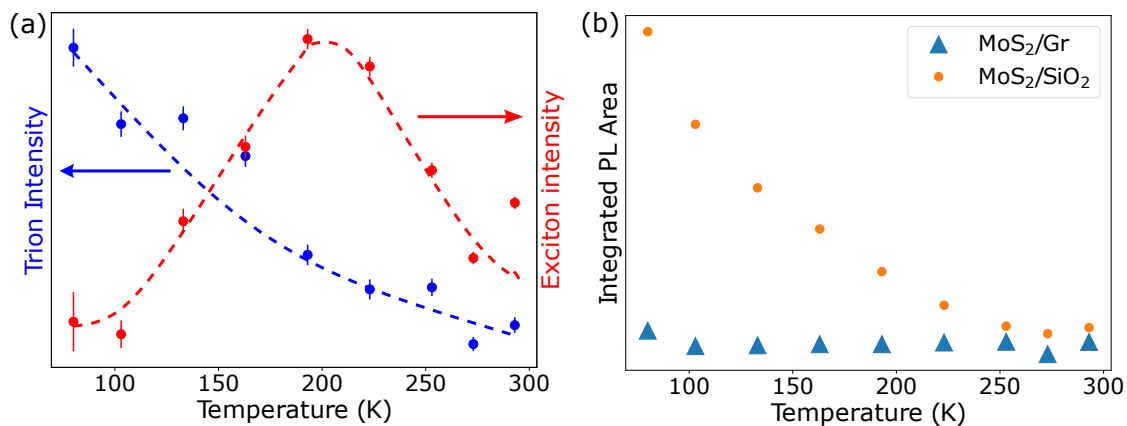


Fig. 3 Salient features of the photocarriers in MoS<sub>2</sub>/FLG heterostructure: (a) Peak intensities of trions (blue) and A excitons (red) formed in MoS<sub>2</sub>/few-layer graphene as a function of temperature. Dashed lines are drawn as a guide to the eye. Trion intensity follows a monotonic behaviour, growing with a decrease in temperature. However, An exciton intensity shows slightly erratic behaviour with an initial increase up to 200 K, then decreases with temperature. (b) Integrated PL area under the curve for MoS<sub>2</sub>/SiO<sub>2</sub> and MoS<sub>2</sub>/FLG as a function of temperature. While the area remains constant for MoS<sub>2</sub>/FLG, it shows a drastic increase in MoS<sub>2</sub>/SiO<sub>2</sub>, which is suggestive of charge transfer mechanisms in the former.

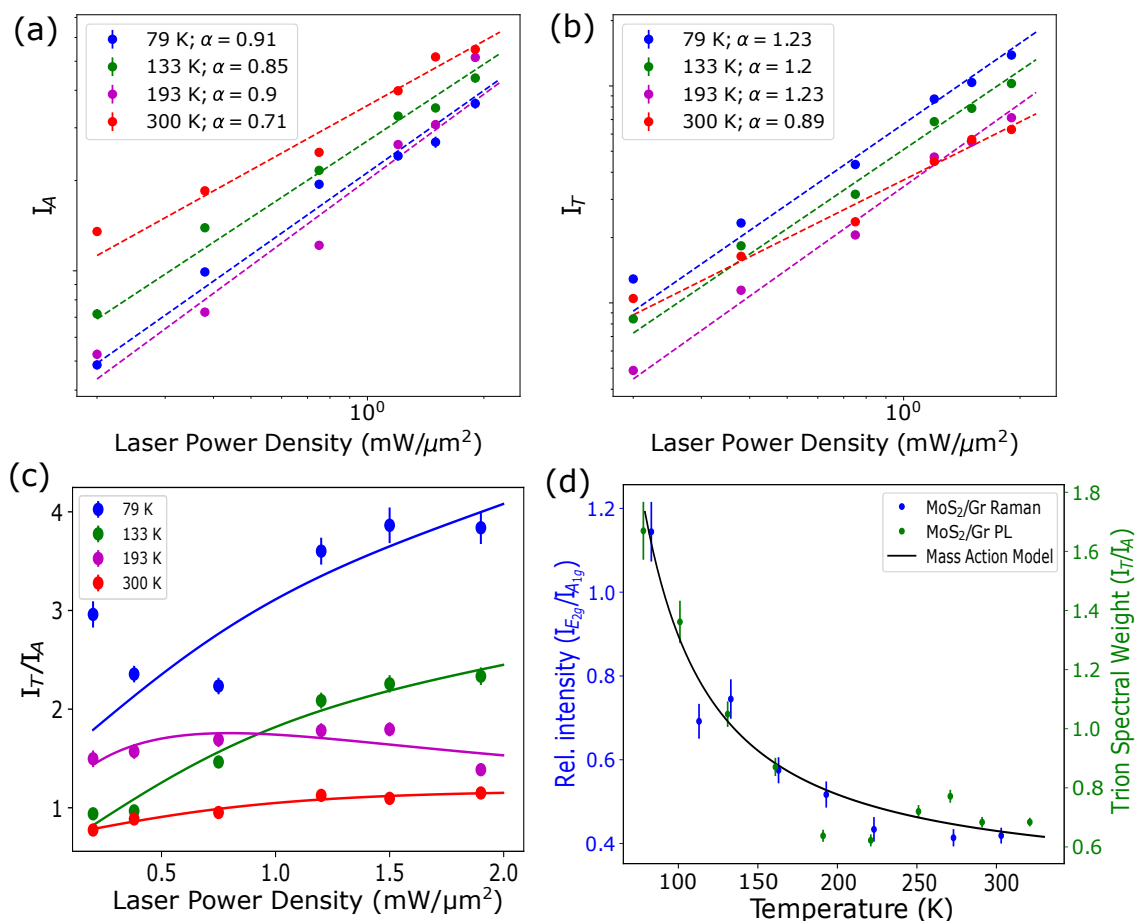


Fig. 4 Control and verification of trion formation: Log-log plots of the measured (a) exciton and (b) trion intensities (in dots) and corresponding fits (in dashed lines) as a function of laser power density ( $P$ ) for 4 different temperatures – 79 K (blue), 133 K (green), 193 K (purple), 300 K (red). The fittings are done with power laws  $P^\alpha$ , where  $P$  is the laser power density. The exponents  $\alpha$  of all fitted power laws are indicated in figure legends. As expected for excitons  $\alpha$  is close to 1 and trions  $\alpha > 1$  (except for 300 K), which obey the power laws. At 300 K, the trion concentration is low due to which there is a discrepancy in the  $\alpha$  values for  $I_A$  and  $I_T$  vs power density fits, i.e., contributions from excitons are dominant in the PL. (c) Measured (dots) and fitted (solid lines) data for relative intensity of trions and excitons ( $I_T/I_A$ ) as a function of laser power density for 4 different temperatures. Fitting was done using Eq. 4. (d) The trion spectral weight ( $I_T/I_A$  - green) of the trion ( $I_T$ ) and exciton ( $I_A$ ) peaks measured from the PL and that of the two Raman modes ( $I_{E_{2g}}/I_{A_{1g}}$  - blue) of MoS<sub>2</sub> are plotted against temperature, for MoS<sub>2</sub>/FLG. It can be seen that both relative intensities follow a similar trend. The temperature-dependent relative intensity measurements were conducted at a power density of  $0.75 \text{ mW}/\mu\text{m}^2$ .

where  $C(T)$  is constant at a fixed temperature  $T$ . Further, as a function of optical pumping (laser intensity)  $I$ , the concentration of negatively charged particles due to electrostatic interaction is<sup>40</sup>:

$$n_T + n_e \propto \tanh(I/I_0) \quad (3)$$

where  $I_0$  is a fitting parameter. Using Eq. 3 in Eq. 2, we get the relative intensity of trions and excitons ( $I_T/I_A$ ) as:

$$\frac{I_T}{I_A} = \frac{A \tanh(\frac{I}{I_0})}{C(T) + BI} \quad (4)$$

where  $A, B, C(T)$  are constants at a fixed temperature. Also, we have taken  $n_A \propto I$ , as  $n_A \gg I_T/I_A$  and is directly proportional to the optical pumping rate. Using Eq. 4 we fit the measured datasets of  $I_T/I_A$  vs. laser power density for 4 different temperatures as shown in Fig. 4 (c). Further, from charge conservation:  $n_e + n_A + 2n_T = n_P + n_B$ . We solve for  $n_T/n_A$  as a function of  $T$  to obtain the mass action model shown in Fig. 4 (d). From the model, we extract the trion binding energy to as  $E_T^b \simeq 15$  meV, matching earlier reports<sup>4</sup>. The background doping levels are close to  $10^{10} \text{ cm}^{-2}$ , i.e., before optical excitation.

To quantify the approximate concentration of charge carriers formed in  $\text{MoS}_2$ , we perform a temperature-dependent Raman measurement for  $\text{MoS}_2$  in the heterostructure [see Fig. S11]. The intensities of the Raman modes are low for  $\text{MoS}_2/\text{FLG}$  as compared to  $\text{MoS}_2/\text{SiO}_2$ , which can be attributed to the substrate-modulated interference effect<sup>18</sup>. At 79 K, we observe a change in the relative intensity of the  $A_{1g}$  w.r.t  $E_{2g}$  mode for  $\text{MoS}_2/\text{FLG}$  only [see Fig. S11, first panel], in comparison to that of 300 K [see Fig. S11, last panel]. Such a quenching of the  $A_{1g}$  mode w.r.t the  $E_{2g}$  mode has been reported earlier by<sup>41</sup>, which is due to electron doping into  $\text{MoS}_2$ . The frequency and linewidth of the  $A_{1g}$  Raman mode change as a function of electron concentration. Since the change in temperature also affects these quantities inversely, due to two competing processes, it is not possible to observe any significant trend in these two quantities. Through the mass action model, we can relate the concentration of trions and excitons, we plot the relative intensity of the Raman peaks to see if electron doping is causing the formation of trions as it would affect the  $A_{1g}$  peak via electron-phonon coupling. Interestingly, we observed that the relative intensity for  $\text{MoS}_2$  in-plane and out-of-plane Raman modes ( $I_{E_{2g}}/I_{A_{1g}}$ ) also obeys the mass-action law and follows the same behaviour as  $I_T/I_A$  from the PL measurement [see Fig. 4 (d)].

We fit the datasets with double Lorentzian to extract quantitative information about the frequencies and linewidths of the Raman modes [refer to Fig. S12 in SI]. The  $A_{1g}$  mode undergoes a stiffening of  $3 \text{ cm}^{-1}$ , whereas the  $E_{2g}$  shows that of  $1 \text{ cm}^{-1}$  [see Fig. S11 (a)-(b)]. The linewidths of both modes remain insensitive to temperature change [see Fig. S12 (c)-(d)]. It is known that  $E_{2g}$  is sensitive to the strain in the material<sup>41–43</sup>. We fitted the linewidth variation of the Raman modes as a function of temperature:  $\omega_X(T) = \omega_X(0) + A_X T$ , where  $\omega_X(0)$  and  $A_X$  are the peak

position at absolute zero temperature and the first-order temperature coefficient for  $X$  ( $X = A_{1g}$  or  $E_{2g}$ ) Raman mode. Note that for both portions of the heterostructure, the linewidths vary with a similar trend and their quantitative difference remains within the error bars. Therefore, we refer to both measurement spots for the following. We obtain the value of  $A_{A_{1g}} = -1.24 \pm 0.1 \times 10^{-2} \text{ cm}^{-1}/\text{K}$ . From  $\Delta\omega_{A_{1g}}$  at  $T = 300 \text{ K}$  and  $T = 79 \text{ K}$ , we estimate the carrier concentration to be  $\approx 10^{13} \text{ cm}^{-2}$  at 79 K, on excitation<sup>41</sup>.

It has been established that the FWHM and peak wavelength of the  $E_{2g}^1$  mode is insensitive to doping or changes in carrier concentration<sup>41</sup>. Thus, in our data, we do not see much change in these parameters of  $E_{2g}^1$  mode. Moreover, the FWHM of  $A_{1g}$  increases for increasing temperature and doping concentration. Thus, these two are competing processes in our measurements, rendering the FWHM of  $A_{1g}$  mode almost constant throughout the measurement. Similarly, for  $E_{2g}^1$  peak, the FLG substrate on which the  $\text{MoS}_2$  flake rests has some undulating surface topology in comparison to  $\text{SiO}_2/\text{Si}$ , which may result in some strain effects. While strain-dependent wavelength shift in  $E_{2g}^1$  mode is a well-studied phenomenon, the amount of strain applied is quite high. Small local strains may go unresolved in a Raman measurement. Thus, here  $E_{2g}^1$  peak does not exhibit any change as many parameters (temperature, doping and local strain) affect its peak parameters in the opposite manner.

There are two main mechanisms that determine trion formation in TMDs: dielectric screening and charge transfer. Next, we discuss the dominant mechanism of these two.

### 3 Discussion: Mechanism

In this section, we describe the two main mechanisms for trion formation: dielectric screening and charge transfer. We also determine which of the two is the dominant cause in trion formation.

#### 3.1 Dielectric Screening

The effect of dielectrics is to screen the Coulomb potential distribution of the interacting charged particles<sup>24</sup>. To illustrate this, we first consider  $\text{SiO}_2$  as a dielectric medium and graphite as a conducting plane which is grounded. The emission occurs in air, which we also consider as a dielectric here, the effective system can be modelled as dielectric/ $\text{MoS}_2$ /dielectric and dielectric/ $\text{MoS}_2$ /conductor for  $\text{MoS}_2/\text{SiO}_2$  and  $\text{MoS}_2/\text{FLG}$ , respectively.

If we consider two charges ( $\pm q_0$ ) in the  $\text{MoS}_2$  layer, separated by a distance  $L$ , then the potential distribution at a point  $(x, z)$  in  $\text{MoS}_2$  is:

$$V(x, z) = \frac{1}{4\pi\epsilon_0 K_s} \left[ \frac{q_0}{\sqrt{(x-L/2)^2 + z^2}} + \frac{-q_0}{\sqrt{(x+L/2)^2 + z^2}} + \sum_{X,n} \frac{q_{X,n}}{\sqrt{(x-x_{X,n})^2 + (z-z_{X,n})^2}} \right] \quad (5)$$

where  $K_s$  is the relative dielectric constant of the  $\text{MoS}_2$  layer,



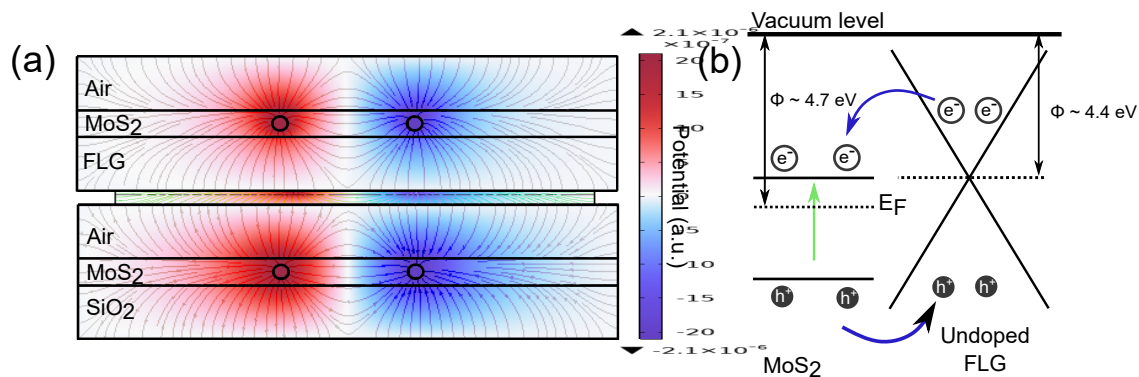


Fig. 5 Mechanism for trion formation: (a) Coulomb potential distribution with an electron (blue circle) and hole (red circle) in the middle layer of the dielectric-sandwich structure (Air/MoS<sub>2</sub>/FLG - top panel; Air/MoS<sub>2</sub>/SiO<sub>2</sub> - bottom panel). The red and blue contours indicate positive and negative electrostatic potential values. (b) Schematic of the band alignment and work functions of MoS<sub>2</sub>/FLG portion of the heterostructure.

$q_{X,n}$  are the image charges in the other layers at  $x_{X,n}, z_{X,n}$  positions w.r.t  $\pm q_0$ . Here we consider two charges ( $\pm q$ ) fixed at  $\pm L/2$  in the MoS<sub>2</sub> layer. Infinite arrays of image charges will be created due to the mirroring of the interfaces between the materials of different dielectric constants. The net potential of the image charges depends on the environmental dielectrics, thereby the screening increases for high- $K$  materials [see Fig. 5 (a)]. The Coulomb potential is screened if the dielectric environment is stronger than the dielectric constant of MoS<sub>2</sub>.

Also, the quasiparticle binding energies provide a measure of the Coulomb interaction strength between the electrons and holes in the material. Trion binding energies in the range of 20 - 40 meV<sup>4,21-24</sup> have been reported in literature for monolayer MoS<sub>2</sub> on SiO<sub>2</sub>. However, it is known that trion binding energy can be affected by substrate dielectric constant<sup>44</sup>, electron density<sup>45</sup> and the distance between the layers of constituent materials in heterostructures<sup>22</sup>. Perebinos et al.<sup>44</sup> suggest that the quasiparticle binding energies ( $\epsilon_X$ ):

$$\epsilon_X \propto (K_{eff})^{-\alpha_X} \quad (6)$$

where  $K_{eff}$  and  $\alpha_X$  are effective dielectric constant of the substrate and environment and empirical constant, respectively.  $X = A$  or  $T$  for A excitons and trions, respectively. The effective dielectric constant,  $K_{eff} = (K_1 + K_2)/2$ , depends on the environmental dielectric constants,  $K_1$  and  $K_2$ , of the top and bottom layers, respectively. Thus, with the increase in the magnitude of the dielectric constant, the binding energy of the quasiparticles decreases.

The dielectric constants of SiO<sub>2</sub> and FLG are  $K_2(\text{SiO}_2) = 4$  and  $K_2(\text{FLG}) = 17$ , respectively. The bottom layers are SiO<sub>2</sub> and FLG thus, the  $K_2$  changes for MoS<sub>2</sub>/SiO<sub>2</sub> and MoS<sub>2</sub>/FLG. Since  $K_{eff} \propto K_2$  and  $\epsilon_X \propto \frac{1}{K_{eff}^{\alpha_X}}$ ,  $K_{eff}(\text{MoS}_2/\text{SiO}_2) < K_{eff}(\text{MoS}_2/\text{FLG})$ . Thus, the trion binding energy reduces for substrates with higher dielectric constants. Further, it has been observed that doping also inversely affects the trion binding energy<sup>45</sup>.

This suggests that optical detection of trions at room temperature should be possible for MoS<sub>2</sub>/SiO<sub>2</sub> as compared to MoS<sub>2</sub>/FLG. However, we do not observe the appearance of trions in MoS<sub>2</sub>/SiO<sub>2</sub>, even upon conducting temperature-dependent measurements down to 79 K. In our system, there are two pos-

sible phenomena which can lead to trion formation – Coulomb potential screening due to the higher dielectric constant of the environment compared to the host material of trions and optically-induced charge transfer from substrate to the host material. In this study, we attempt to identify the dominant mechanism for trion formation as this has been a matter of debate<sup>22</sup>. Since we do not observe trion formation in MoS<sub>2</sub>/SiO<sub>2</sub>, where the phenomenon of dielectric screening should facilitate charge transfer, we conclude that the former is not the dominant mechanism for trion formation. Rather, charge transfer (which is relatively higher for MoS<sub>2</sub>/FLG as compared to MoS<sub>2</sub>/SiO<sub>2</sub>) is the relevant phenomenon causing trion formation. Thus, there must be local doping effects in MoS<sub>2</sub> via FLG due to which were observed trions in MoS<sub>2</sub>/FLG.

### 3.2 Charge Transfer

Doping from one material to another can occur due to a mismatch of work functions. The work function of few-layer graphene (in our case, close to 6 layers is  $\phi_{FLG} \simeq 4.4$  eV) is lower than that of monolayer MoS<sub>2</sub> ( $\phi_{MS} \simeq 4.7$  eV) [see Fig. 5 (b)]. This allows a spontaneous transfer of electrons from FLG to MoS<sub>2</sub>. Non-radiative energy transfer (NRET) has been extensively studied and typically involves either Coulombic interactions (Förster-type) or electronic exchange. Usually, for Coulombic interactions, both participating materials should be photoluminescent. Thus, in our system electronic exchange occurs due to a mismatch of work functions.

## 4 Conclusion

Summarising, we have illustrated the temperature-dependent charge transfer mechanism in MoS<sub>2</sub>/FLG heterostructure. Raman and PL spectroscopy show the selective formation of trions on MoS<sub>2</sub> supported by few-layer graphene. Trion concentration increases with a decrease in temperature obeying the mass-action law. Further, with an increase in excitation power, the trion concentration can be tuned. The binding energy ( $\simeq 15$  meV) of the trions formed in MoS<sub>2</sub>/FLG was calculated using the mass action model. We also highlight the effect of substrate dielectrics on the probability of trion observation. Through this, we argue that



charge transfer and Coulomb potential screening are the possible mechanisms behind trion formation. Most effectively, the increase in carrier concentration is a dominant factor in trion formation. This present work provides an efficient approach for trion formation in MoS<sub>2</sub>/FLG and tuning its concentration, which has potential applications in optoelectronics and light detection.

## 5 Experimental Methods

### 5.1 Sample preparation

Graphite flakes were mechanically exfoliated. Monolayer MoS<sub>2</sub> flakes on 290 nm SiO<sub>2</sub>/Si substrates were grown via chemical vapour deposition (CVD), similar to<sup>46</sup>. In a typical run, Sulphur (S, Sigma Aldrich 99.98%) and Molybdenum oxide (MoO<sub>3</sub>, Alfa Aesar, 99%) powders were used as precursors. 4 mg MoO<sub>3</sub> powder was kept in the middle of the chamber at 825 °C and 315 mg S was kept 35 cm upstream from it at 285 °C. 100 SCCM Ar was used as a carrier and purging gas. Purging and growth were carried out for 15 and 45 minutes, respectively, in an Ar environment.

For heterostructure fabrication, the as-grown monolayer MoS<sub>2</sub> flakes were dry-transferred onto graphite flakes using a polydimethylsiloxane (PDMS) stamp and a thin film of polycarbonate. The heterostructure consists of a part of the MoS<sub>2</sub> on the graphite flake [which is 4 nm thick and thus, is referred to as few-layer graphene] and the remaining lies on the SiO<sub>2</sub> substrate.

### 5.2 Measurements

Raman and PL spectroscopic measurements were performed using a confocal Raman spectrometer (Renishaw, inVia Reflex). The spectrometer has a back-scattering geometry under 532 nm laser excitation. The measurements were carried out with a 50× (NA 0.55) objective with a long working distance. The laser has a focal spot size of 1 μm, and the spectrum was collected using 600[1800] lines per mm grating for the PL[Raman] measurements. The sample was placed in a liquid nitrogen-cooled Linkam cryostat for temperature-dependent measurement. The laser power was kept around 300 μW during the temperature-dependent measurements, and for power-dependent measurements, it was kept below 2 mW to avoid local heating.

### Author Contributions

M.G.D. performed measurements, analyzed the data and wrote the manuscript. N.B. performed the CVD growth of the monolayer TMD sample. M.G.D and I.K. fabricated the heterostructure. J.K., P.K.N., S.S. and V.P.B. edited the manuscript, discussed the implications of the results and supervised the overall project.

### Conflicts of interest

The Authors declare no competing financial or non-financial interests.

## 6 Acknowledgments

I-H. K., J.K., and S.S. acknowledge the funding from the Center for Emergent Materials at Ohio State University, a National Science Foundation (NSF) MRSEC through Award No. DMR-

2011876. J.K. also acknowledges the funding from the U.S. Department, Office of Science, Office of Basic Sciences, of the U.S. Department of Energy under Award No. DE-SC0020323. V.P.B. and P.K.N. acknowledge MHRD STARS research grant [STARS/APR2019/396]. M.G.D. acknowledges the support from the Prime Minister's Research Fellowship (PMRF), India. V.P.B., P.K.N. and M.G.D. acknowledge the support from the Institute of Eminence scheme.

## Notes and references

- 1 M. Chhowalla, H. S. Shin, G. Eda, L.-J. Li, K. P. Loh and H. Zhang, *Nat. Chem.*, 2013, **5**, 263–275.
- 2 Y. Yoon, K. Ganapathi and S. Salahuddin, *Nano Lett.*, 2011, **11**, 3768–3773.
- 3 J. Xiao, M. Zhao, Y. Wang and X. Zhang, *Nanophotonics*, 2017, **6**, 1309–1328.
- 4 K. F. Mak, K. He, C. Lee, G. H. Lee, J. Hone, T. F. Heinz and J. Shan, *Nat. Mater.*, 2013, **12**, 207–211.
- 5 K. De Greve, L. Yu, P. L. McMahon, J. S. Pelc, C. M. Natarajan, N. Y. Kim, E. Abe, S. Maier, C. Schneider, M. Kamp *et al.*, *Nature*, 2012, **491**, 421–425.
- 6 D. Brinkmann, J. Kudrna, P. Gilliot, B. Hönerlage, A. Arnoult, J. Cibert and S. Tatarenko, *Phys. Rev. B*, 1999, **60**, 4474.
- 7 J. Puls, G. Mikhailov, F. Henneberger, D. Yakovlev, A. Waag and W. Faschinger, *Phys. Rev. Lett.*, 2002, **89**, 287402.
- 8 Y. Zhang, T. Oka, R. Suzuki, J. Ye and Y. Iwasa, *Science*, 2014, **344**, 725–728.
- 9 J. Pei, J. Yang, R. Xu, Y.-H. Zeng, Y. W. Myint, S. Zhang, J.-C. Zheng, Q. Qin, X. Wang, W. Jiang *et al.*, *Small*, 2015, **11**, 6384–6390.
- 10 H. Chen, M. B. Müller, K. J. Gilmore, G. G. Wallace and D. Li, *Adv. Mater.*, 2008, **20**, 3557–3561.
- 11 K. Lee, H.-Y. Kim, M. Lotya, J. N. Coleman, G.-T. Kim and G. S. Duesberg, *Adv. Mater.*, 2011, **23**, 4178–4182.
- 12 X.-Y. Yu, H. Hu, Y. Wang, H. Chen and X. W. Lou, *Angew. Chem.*, 2015, **127**, 7503–7506.
- 13 H. Liu, S. L. Wong and D. Chi, *Chemical Vapor Deposition*, 2015, **21**, 241–259.
- 14 C.-P. Lu, G. Li, K. Watanabe, T. Taniguchi and E. Y. Andrei, *Phys. Rev. Lett.*, 2014, **113**, 156804.
- 15 A. K. Rocha Robledo, M. Flores Salazar, B. A. Muñoz Martínez, Á. A. Torres-Rosales, H. F. Lara-Alfaro, O. Del Pozo-Zamudio, E. A. Cerda-Méndez, S. Jiménez-Sandoval and A. De Luna Bugallo, *Plos one*, 2023, **18**, e0283834.
- 16 M. Yang, L. Wang, G. Hu, X. Chen, P. L. Gong, X. Cong, Y. Liu, Y. Yang, X. Li, X. Zhao *et al.*, *Nano Res.*, 2021, **14**, 2241–2246.
- 17 Z. Melnikova-Kominkova, K. Jurkova, V. Vales, K. Drogowska-Horná, O. Frank and M. Kalbac, *Physical Chemistry Chemical Physics*, 2019, **21**, 25700–25706.
- 18 M. Buscema, G. A. Steele, H. S. Van Der Zant and A. Castellanos-Gomez, *Nano Res.*, 2014, **7**, 561–571.
- 19 A. Nipane, D. Karmakar, N. Kaushik, S. Karande and S. Lodha, *ACS Nano*, 2016, **10**, 2128–2137.
- 20 S. Mouri, Y. Miyauchi and K. Matsuda, *Nano Lett.*, 2013, **13**,

- 5944–5948.
- 21 S. Golovynskyi, O. I. Datsenko, D. Dong, Y. Lin, I. Irfan, B. Li, D. Lin and J. Qu, *J. Phys. Chem. C*, 2021, **125**, 17806–17819.
  - 22 M. Florian, M. Hartmann, A. Steinhoff, J. Klein, A. W. Holleitner, J. J. Finley, T. O. Wehling, M. Kaniber and C. Gies, *Nano Lett.*, 2018, **18**, 2725–2732.
  - 23 J. S. Ross, S. Wu, H. Yu, N. J. Ghimire, A. M. Jones, G. Aivazian, J. Yan, D. G. Mandrus, D. Xiao, W. Yao *et al.*, *Nat. Commun.*, 2013, **4**, 1474.
  - 24 Y. Lin, X. Ling, L. Yu, S. Huang, A. L. Hsu, Y.-H. Lee, J. Kong, M. S. Dresselhaus and T. Palacios, *Nano Lett.*, 2014, **14**, 5569–5576.
  - 25 M. A. Pimenta, E. Del Corro, B. R. Carvalho, C. Fantini and L. M. Malard, *Acc. Chem. Res.*, 2015, **48**, 41–47.
  - 26 X. Ling, L. Xie, Y. Fang, H. Xu, H. Zhang, J. Kong, M. S. Dresselhaus, J. Zhang and Z. Liu, *Nano Lett.*, 2010, **10**, 553–561.
  - 27 S. Kim, S. Park, H. Kim, G. Jang, D. Park, J.-Y. Park, S. Lee and Y. Ahn, *Appl. Phys. Lett.*, 2016, **108**, –.
  - 28 J. W. Christopher, B. B. Goldberg and A. K. Swan, *Sci. Rep.*, 2017, **7**, 14062.
  - 29 K. M. McCreary, A. T. Hanbicki, S. V. Sivaram and B. T. Jonker, *APL Mater.*, 2018, **6**, –.
  - 30 F. J. Crowne, M. Amani, A. G. Birdwell, M. L. Chin, T. P. O'Regan, S. Najmaei, Z. Liu, P. M. Ajayan, J. Lou and M. Dubey, *Phys. Rev. B Condens. Matter*, 2013, **88**, 235302.
  - 31 S. Tongay, J. Zhou, C. Ataca, K. Lo, T. S. Matthews, J. Li, J. C. Grossman and J. Wu, *Nano Lett.*, 2012, **12**, 5576–5580.
  - 32 K. P. O'donnell and X. Chen, *Appl. Phys. Lett.*, 1991, **58**, 2924–2926.
  - 33 S. Tongay, J. Zhou, C. Ataca, J. Liu, J. S. Kang, T. S. Matthews, L. You, J. Li, J. C. Grossman and J. Wu, *Nano Lett.*, 2013, **13**, 2831–2836.
  - 34 Y. V. Zhumagulov, A. Vagov, D. R. Gulevich, P. E. Faria Junior and V. Perebeinos, *J. Chem. Phys.*, 2020, **153**, –.
  - 35 I. Paradisanos, S. Germanis, N. Pelekanos, C. Fotakis, E. Ky-makis, G. Kioseoglou and E. Stratakis, *Appl. Phys. Lett.*, 2017, **110**, –.
  - 36 Y. You, X.-X. Zhang, T. C. Berkelbach, M. S. Hybertsen, D. R. Reichman and T. F. Heinz, *Nat. Phys.*, 2015, **11**, 477–481.
  - 37 D. Kaplan, Y. Gong, K. Mills, V. Swaminathan, P. Ajayan, S. Shirodkar and E. Kaxiras, *2D Mater.*, 2016, **3**, 015005.
  - 38 A. Arora, P. K. Nayak, T. Dixit, K. L. Ganapathi, A. Krishnan and M. S. R. Rao, *Nanophotonics*, 2020, **9**, 3881–3887.
  - 39 A. Vercik, Y. G. Gobato and M. Brasil, *J. Appl. Phys.*, 2002, **92**, 1888–1892.
  - 40 J. Siviniant, D. Scalbert, A. Kavokin, D. Coquillat and J. Lascaray, *Phys. Rev. B*, 1999, **59**, 1602.
  - 41 B. Chakraborty, A. Bera, D. Muthu, S. Bhowmick, U. V. Waghmare and A. Sood, *Phys. Rev. B*, 2012, **85**, 161403.
  - 42 N. Basu, R. Kumar, D. Manikandan, M. G. Dastidar, P. Hedge, P. K. Nayak and V. P. Bhallamudi, *RSC Adv.*, 2023, **13**, 16241–16247.
  - 43 C. Rice, R. Young, R. Zan, U. Bangert, D. Wolverson, T. Georgiou, R. Jalil and K. Novoselov, *Phys. Rev. B*, 2013, **87**, 081307.
  - 44 V. Perebeinos, J. Tersoff and P. Avouris, *Phys. Rev. Lett.*, 2004, **92**, 257402.
  - 45 C. Zhang, H. Wang, W. Chan, C. Manolatou and F. Rana, *Phys. Rev. B*, 2014, **89**, 205436.
  - 46 E. M. Alexeev, A. Catanzaro, O. V. Skrypka, P. K. Nayak, S. Ahn, S. Pak, J. Lee, J. I. Sohn, K. S. Novoselov, H. S. Shin *et al.*, *Nano Lett.*, 2017, **17**, 5342–5349.

## **Data Availability Statement**

Data for this article will be uploaded to a standard public repository upon acceptance, in accordance with the journal guidelines.